Dark Matter Search Results from a One Tonne×Year Exposure of XENON1T

E. Aprile,[1] J. Aalbers,[2] F. Agostini,[3] M. Alfonsi,[4] L. Althueser,[5] F. D. Amaro,[6] M. Anthony,[1] F. Arneodo,[7] L. Baudis,[8] B. Bauermeister,[9] M. L. Benabderrahmane,[7] T. Berger,[10] P. A. Breur,[2] A. Brown,[2] A. Brown,[8] E. Brown,[10] S. Bruenner,[11] G. Bruno,[7] R. Budnik,[12] C. Capelli,[8] J. M. R. Cardoso,[6] D. Cichon,[11] D. Coderre,[13,*] A. P. Colijn,[2] J. Conrad,[9] J. P. Cussonneau,[14] M. P. Decowski,[2] P. de Perio,[1,†] P. Di Gangi,[3] A. Di Giovanni,[7] S. Diglio,[14] A. Elykov,[13] G. Eurin,[11] J. Fei,[15] A. D. Ferella,[9] A. Fieguth,[5] W. Fulgione,[16,17] A. Gallo Rosso,[16] M. Galloway,[8] F. Gao,[1,‡] M. Garbini,[3] C. Geis,[4] L. Grandi,[18] Z. Greene,[1] H. Qiu,[12] C. Hasterok,[11] E. Hogenbirk,[2] J. Howlett,[1] R. Itay,[12] F. Joerg,[11] B. Kaminsky,[13,§] S. Kazama,[8,¶] A. Kish,[8] G. Koltman,[12] H. Landsman,[12] R. F. Lang,[19] L. Levinson,[12] Q. Lin,[1] S. Lindemann,[13] M. Lindner,[11] F. Lombardi,[15] J. A. M. Lopes,[6,**] J. Mahlstedt,[9] A. Manfredini,[12] T. Marrodán Undagoitia,[11] J. Masbou,[14] D. Masson,[19] M. Messina,[7] K. Micheneau,[14] K. Miller,[18] A. Molinario,[16] K. Morå,[9] M. Murra,[5] J. Naganoma,[20] K. Ni,[15] U. Oberlack,[4] B. Pelssers,[9] F. Piastra,[8] J. Pienaar,[18] V. Pizzella,[11] G. Plante,[1] R. Podviianiuk,[16] N. Priel,[12] D. Ramírez García,[13] L. Rauch,[11] S. Reichard,[8] C. Reuter,[19] B. Riedel,[18] A. Rizzo,[1] A. Rocchetti,[13] N. Rupp,[11] J. M. F. dos Santos,[6] G. Sartorelli,[3] M. Scheibelhut,[4] S. Schindler,[4] J. Schreiner,[11] D. Schulte,[5] M. Schumann,[13] L. Scotto Lavina,[21] M. Selvi,[3] P. Shagin,[20] E. Shockley,[18] M. Silva,[6] H. Simgen,[11] D. Thers,[14] F. Toschi,[3,13] G. Trinchero,[17] C. Tunnell,[18] N. Upole,[18] M. Vargas,[5] O. Wack,[11] H. Wang,[22] Z. Wang,[16] Y. Wei,[15] C. Weinheimer,[5] C. Wittweg,[5] J. Wulf,[8] J. Ye,[15] Y. Zhang,[1] and T. Zhu[1]

(XENON Collaboration),[††]

[1]*Physics Department, Columbia University, New York, NY 10027, USA*
[2]*Nikhef and the University of Amsterdam, Science Park, 1098XG Amsterdam, Netherlands*
[3]*Department of Physics and Astronomy, University of Bologna and INFN-Bologna, 40126 Bologna, Italy*
[4]*Institut für Physik & Exzellenzcluster PRISMA, Johannes Gutenberg-Universität Mainz, 55099 Mainz, Germany*
[5]*Institut für Kernphysik, Westfälische Wilhelms-Universität Münster, 48149 Münster, Germany*
[6]*LIBPhys, Department of Physics, University of Coimbra, 3004-516 Coimbra, Portugal*
[7]*New York University Abu Dhabi, Abu Dhabi, United Arab Emirates*
[8]*Physik-Institut, University of Zurich, 8057 Zurich, Switzerland*
[9]*Oskar Klein Centre, Department of Physics, Stockholm University, AlbaNova, Stockholm SE-10691, Sweden*
[10]*Department of Physics, Applied Physics and Astronomy, Rensselaer Polytechnic Institute, Troy, NY 12180, USA*
[11]*Max-Planck-Institut für Kernphysik, 69117 Heidelberg, Germany*
[12]*Department of Particle Physics and Astrophysics, Weizmann Institute of Science, Rehovot 7610001, Israel*
[13]*Physikalisches Institut, Universität Freiburg, 79104 Freiburg, Germany*
[14]*SUBATECH, IMT Atlantique, CNRS/IN2P3, Université de Nantes, Nantes 44307, France*
[15]*Department of Physics, University of California, San Diego, CA 92093, USA*
[16]*INFN-Laboratori Nazionali del Gran Sasso and Gran Sasso Science Institute, 67100 L'Aquila, Italy*
[17]*INFN-Torino and Osservatorio Astrofisico di Torino, 10125 Torino, Italy*
[18]*Department of Physics & Kavli Institute for Cosmological Physics, University of Chicago, Chicago, IL 60637, USA*
[19]*Department of Physics and Astronomy, Purdue University, West Lafayette, IN 47907, USA*
[20]*Department of Physics and Astronomy, Rice University, Houston, TX 77005, USA*
[21]*LPNHE, Université Pierre et Marie Curie, Université Paris Diderot, CNRS/IN2P3, Paris 75252, France*
[22]*Physics & Astronomy Department, University of California, Los Angeles, CA 90095, USA*

(Dated: August 14, 2018)

We report on a search for Weakly Interacting Massive Particles (WIMPs) using 278.8 days of data collected with the XENON1T experiment at LNGS. XENON1T utilizes a liquid xenon time projection chamber with a fiducial mass of (1.30 ± 0.01) t, resulting in a 1.0 t×yr exposure. The energy region of interest, [1.4, 10.6] keV$_{ee}$ ([4.9, 40.9] keV$_{nr}$), exhibits an ultra-low electron recoil background rate of $(82^{+5}_{-3}\,(\text{sys}) \pm 3\,(\text{stat}))$ events/(t × yr × keV$_{ee}$). No significant excess over background is found and a profile likelihood analysis parameterized in spatial and energy dimensions excludes new parameter space for the WIMP-nucleon spin-independent elastic scatter cross-section for WIMP masses above 6 GeV/c^2, with a minimum of 4.1×10^{-47} cm^2 at 30 GeV/c^2 and 90% confidence level.

PACS numbers: 95.35.+d, 14.80.Ly, 29.40.-n, 95.55.Vj
Keywords: Dark Matter, Direct Detection, Xenon

An abundance of astrophysical observations suggests the existence of a non-luminous, massive component of the universe called dark matter (DM) [1, 2]. The Weakly Interacting Massive Particle (WIMP) is one of the most promising DM candidates, motivating numerous terrestrial and astronomical searches [3, 4]. The most suc-

cessful class of direct detection experiments searching for WIMPs with masses between a few GeV/c^2 to TeV/c^2 have utilized liquid xenon (LXe) time projection chambers (TPCs) and set stringent limits on the coupling of WIMPs to matter, excluding the WIMP-nucleon spin-independent elastic cross-section, σ_{SI}, for a 30 GeV/c^2 WIMP to below 10^{-46} cm^2 [5–7].

The XENON1T experiment [8], located at an average depth of 3600 m water-equivalent at the INFN Laboratori Nazionali del Gran Sasso (LNGS), is the largest such detector to date containing 3.2 t of ultra-pure LXe with 2 t employed as the target material in the active volume. This PTFE-lined, 96 cm diameter cylinder is instrumented above and below by arrays of 127 and 121 Hamamatsu R11410-21 3" photomultiplier tubes (PMTs) [9, 10]. A particle incident on the LXe target deposits energy that produces a prompt scintillation signal (S1) and ionization electrons. The active volume is defined by a cathode and a grounded gate electrode separated by 97 cm to provide a drift field for the electrons. These electrons are extracted into gaseous xenon (GXe) where they produce proportional scintillation light (S2) via electroluminescence through a $\gtrsim$ 10 kV/cm multiplication field. The S2/S1 size ratio allows for discrimination between nuclear recoils (NRs; from WIMPs or neutrons) and electronic recoils (ERs; from β or γ). The time delay between S1 and S2 and the localization of the S2 pattern in the top PMT array indicate the vertical and horizontal position of the interaction, respectively. The detector is surrounded by an active water Cherenkov muon veto system [11].

This DM search combines data from two science runs which spanned from November 22, 2016 to January 18, 2017 (SR0 [5], re-analyzed in this work) and February 2, 2017 to February 8, 2018 (SR1), with the brief interruption due to an earthquake. The livetime is reduced by 7.8% (1.2%) for SR0 (SR1) when the data acquisition system was insensitive to new events, 1.2% when the muon veto was either disabled or triggered in coincidence with the TPC, and 4.4% after high-energy events in the TPC that induced photo-ionization and delayed electron extraction activity [12], resulting in 32.1 days and 246.7 days for SR0 and SR1, respectively. The two science runs differ in the cathode voltage of -12 kV (SR0) and -8 kV (SR1), corresponding to drift fields of 120 V/cm and 81 V/cm, with position-dependent variations of 2.2 V/cm RMS based on a field map derived with the KEMField simulation package [13] and cross-checked by a data-driven method. The LXe level is maintained at 2.5 mm above the gate electrode, within sensor reading fluctuations of 2% RMS. The LXe temperature and GXe pressure were constant at $-96.0\,^{\circ}$C and 1.94 bar, both with $< 0.02\%$ RMS. For this analysis, 36 PMTs are ignored due to vacuum leaks or low single photo-electron (SPE) acceptance [8].

Several internal and external radioactive sources were deployed to calibrate the detector. ^{83m}Kr calibration data [14] were collected every $\sim$2.5 weeks to monitor various detector parameters. Low-energy ERs are calibrated with 17.1 days of data taken with an internal ^{220}Rn source [15], split into seven periods spread throughout the science runs. NR calibration is performed with 30.0 days of exposure to an external ^{241}AmBe source, roughly split between science runs, and 1.9 days of exposure to a D-D neutron generator [16] in SR1.

Each PMT channel is continuously digitized at a rate of 100 MHz. The PMT gains range from $(1-5)\times10^6$ and signals above a minimum threshold of 2.06 mV are recorded as "hits" resulting in a mean SPE acceptance of 93% with a standard deviation of 3% across all active channels. A software trigger searches in time for clusters of hits compatible with S1 or S2 signals and saves the duration corresponding to the maximum drift time ($\sim$700 μs) around them. This data is simultaneously backed up to tape and transferred to external grid sites where it is processed [17] with the PAX reconstruction software package [8, 18].

PMT signals are corrected for time-dependent gains. The gains are monitored weekly with a pulsed LED configured to produce signals of a few photoelectrons (PE) [19] and are stable within 1-2% throughout each science run, except in a small number of PMTs whose voltages were intentionally lowered due to diffusive leaks or which experienced dynode deterioration. S1 signals are corrected (cS1) for position-dependent light collection efficiency (LCE) due to geometric effects, measured in ^{83m}Kr calibration data and showing a maximum deviation of 80%. While drifting through LXe, electrons can be captured by electronegative impurities and thus the S2 size must be corrected for electron lifetime, which is measured with high time-granularity using α-decays from ^{222}Rn daughters during DM search data-taking as well as with ^{83m}Kr calibration data. The electron lifetime increased from 380 μs at the beginning of SR0 to a plateau of $\sim$650 μs at the end of SR1 due to decreased outgassing over time and continuous GXe purification through hot getters. S2 signals are additionally corrected (cS2) for position-dependent LCE and inhomogeneous electroluminescence amplification, a maximum effect of 32% from the edge of the TPC to center. The bottom PMT array ($cS2_b$) is used for S2 energy reconstruction due to a more spatially homogeneous LCE.

Position reconstruction in the horizontal plane employs an artificial neural network trained with simulated S2 top-array PMT hit-patterns. This Monte Carlo (MC) simulation includes the full detector geometry, optical photon propagation, PMT quantum efficiencies, multiple-PE emission by one photon [20], and gains. Optical parameters are tuned to match the S1 LCE and the fraction of the S2 signal in the top-array in ^{83m}Kr data. Drift field distortion causes an inward shift of the reconstructed position and is corrected using ^{83m}Kr data to

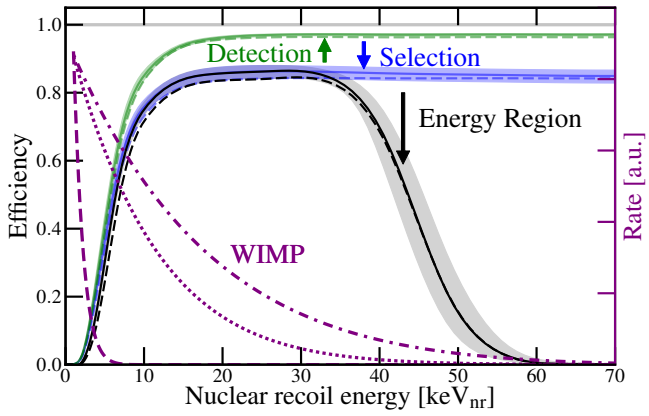

FIG. 1: Best-fit total efficiencies (black), including the energy ROI selection, for SR0 (dashed) and SR1 (solid) as a function of true NR energy (keV$_{nr}$). The efficiency of S1 detection (green) and that of S1 detection and selection (blue) are shown. The shaded bands show the 68% credible regions for SR1. The expected spectral shapes (purple) of 10 GeV/c^2 (dashed), 50 GeV/c^2 (dotted), and 200 GeV/c^2 (dashed dotted) WIMPs are overlaid for reference.

obtain the horizontal (X and Y, giving radius, R) and vertical (Z) interaction positions. The bottom of the TPC (Z = −96.9 cm) shows the largest radial bias of 7.7 cm (12.2 cm) at the beginning (end) of DM search data taking, with time-dependence mostly due to gradual charge accumulation on the PTFE surfaces, similar to the observation by [21]. The resulting position distributions of both spatially homogeneous ^{222}Rn-chain α-decays and ^{131m}Xe decays, as well as localized NRs from external ^{241}AmBe and neutron generator calibration data, agree well with MC and validate this correction procedure.

The DM search data was blinded (SR0 re-blinded after the publication of [5]) in the signal region above the S2 threshold of 200 PE and below the ER -2σ quantile in (cS1, cS2$_b$) space, prior to the tuning and development of event selection criteria and signal and background models. Data quality criteria are imposed to include only well-reconstructed events and to suppress known backgrounds. All events must contain a valid S1 and S2 pair. S1s are required to contain coincident signals from at least 3 PMTs within 100 ns. The energy region of interest (ROI) is defined by cS1 between 3 and 70 PE, corresponding to an average [1.4, 10.6] keV$_{ee}$ (ER energy) or [4.9, 40.9] keV$_{nr}$ (NR energy). Furthermore, in order to suppress low-energy accidental coincidence (AC) events, S1 candidates must not have shape properties compatible with S2 signals produced by single electrons. The resulting S1 detection efficiency, estimated by simulation, is shown in Fig. 1 and is smaller than that in [5] due to a wider S1 shape in the simulation tuned to ^{83m}Kr and ^{220}Rn data as well as properly accounting for misclassification as S2. This efficiency is consistent with that obtained by a data-driven method where small S1s are simulated via bootstrapping PMT hits from 20-100 PE S1s.

The signal ratio between the top and bottom PMT arrays is dependent on the depth at which the light is produced. For an S1 at a given interaction position, a p-value is computed based on the observed and expected top/bottom ratio and p-values < 0.001 are rejected. S2s are produced at the liquid-gas interface and thus must have a compatible fraction of light seen in the top array of ∼63%. To reject events coming from occasional light emission from malfunctioning PMTs, a threshold is placed on the maximum fractional contribution of a single PMT to an S1 signal.

The likelihoods of both the S1 and S2 observed hit-patterns compared to those expected from simulation, given the reconstructed position, are used to reject events that may be a result of multiple-scatters or AC. The low-cS2$_b$, cS1 = 68 PE, event found in [5] did not pass event selection criteria in this analysis due to improvements to the MC simulation used for the S2 hit-pattern likelihood. To suppress events with poorly reconstructed hit-patterns that occur in regions with a high density of inactive PMT channels, the difference between the neural network and a likelihood-fit algorithm is required to be less than 2 to 5 cm, tighter towards larger S2 where fluctuations become negligible. As in [5], the width of the S2 signal in time must be compatible with the depth of the interaction, and the multiplicity of S1 and S2 signals must be consistent with a single-scatter event. The efficiency of all selection conditions is shown in Fig. 1, estimated using a combination of simulations and calibration control samples.

This analysis expands on that in [5] by modeling the radial distribution in the statistical inference procedure and categorizing events at inner radii based on Z, such that the analysis space is cS1, cS2$_b$, R, and Z. Each background component described below, and the WIMP NR signal, are modeled as a probability density function of all analysis dimensions. For WIMP NR energy spectra, the Helm form factor for the nuclear cross section [22] and a standard isothermal DM halo as in [5] are assumed, with $v_0 = 220$ km/s, $\rho_{DM} = 0.3$ GeV/(c$^2 \times$ cm^3), $v_{esc} = 544$ km/s, and Earth velocity of $v_E = 232$ km/s. These spectra are converted into the analysis space via the detector model described below. Figures 2 and 3 show the background and signal model shapes in various 2D projections of the analysis space compared to data. The 1D projection in Fig. 4 and integrals in Table I show the absolute rate comparisons. An NR signal reference region is defined between the 200 GeV/c^2 WIMP median and -2σ quantile in (cS2$_b$, cS1) space.

The ^{nat}Kr concentration in LXe is reduced via cryogenic distillation [23] to a sub-dominant level of ^{nat}Kr/Xe = (0.66±0.11) ppt, as determined from regular mass-spectrometry measurements [24], and contributes an ER background rate of (7.7 ± 1.3) events/(t × yr ×

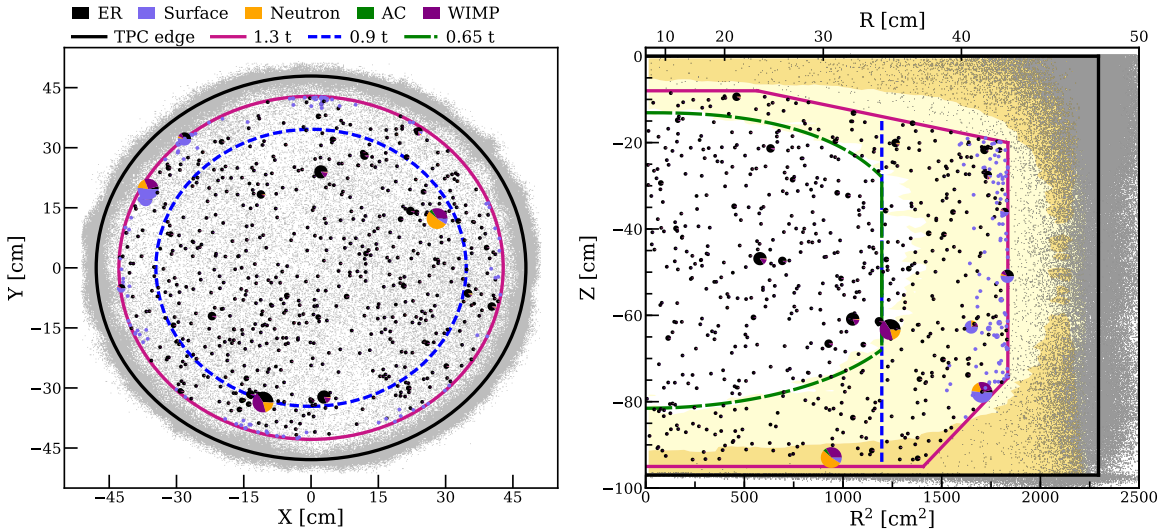

FIG. 2: Spatial distributions of DM search data. Events that pass all selection criteria and are within the fiducial mass are drawn as pie charts representing the relative probabilities of the background and signal components for each event under the best-fit model (assuming a 200 GeV/c^2 WIMP and resulting best-fit $\sigma_{SI} = 4.7 \times 10^{-47}$ cm^2) with color code given in the legend. Small charts (mainly single-colored) correspond to unambiguously background-like events, while events with larger WIMP probability are drawn progressively larger. Gray points are events reconstructed outside the fiducial mass. The TPC boundary (black line), 1.3 t fiducial mass (magenta), maximum radius of the reference 0.9 t mass (blue dashed), and 0.65 t core mass (green dashed) are shown. Yellow shaded regions display the 1σ (dark), and 2σ (light) probability density percentiles of the radiogenic neutron background component for SR1.

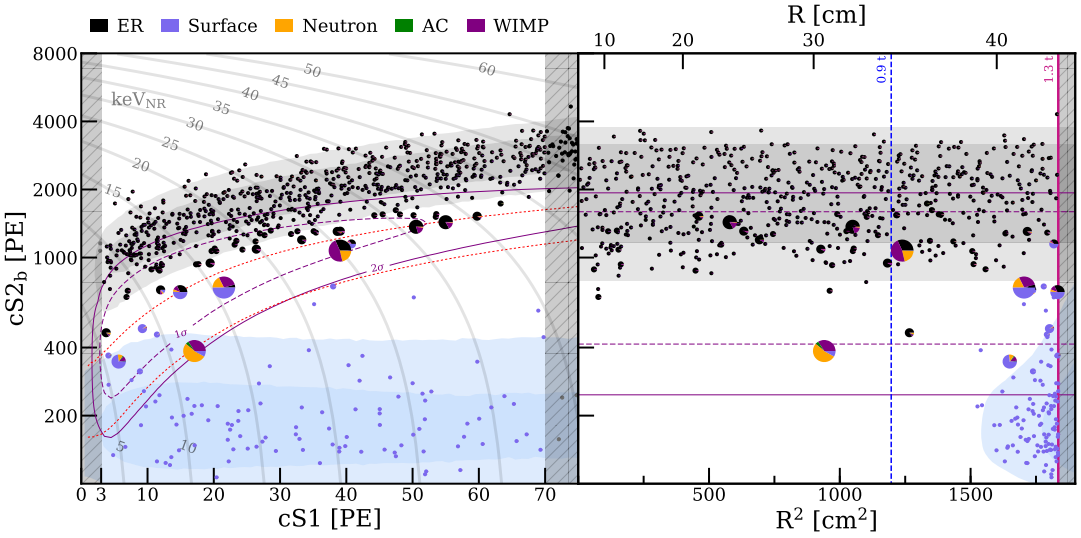

FIG. 3: DM search data in the 1.3 t fiducial mass distributed in (cS1, cS2$_b$) (left) and (R^2, cS2$_b$) (right) parameter spaces with the same marker descriptions as in Fig. 2. Shaded regions are similar to Fig. 2, showing the projections in each space of the surface (blue) and ER (gray) background components for SR1. The 1σ (purple dashed) and 2σ (purple solid) percentiles of a 200 GeV/c^2 WIMP signal are overlaid for reference. Vertical shaded regions are outside the ROI. The NR signal reference region (left, between the two red dotted lines) and the maximum radii (right) of the 0.9 t (blue dashed) and 1.3 t (magenta solid) masses are shown. Gray lines show iso-energy contours in NR energy.

keV$_{ee}$). The background contribution from the natural radioactivity of detector materials is suppressed within the fiducial volume to a similar level. Thus, the dominant ER background is from β-decays of ^{214}Pb originating from ^{222}Rn emanation. The maximum and minimum decay rate of ^{214}Pb is (12.6±0.8) and (5.1±0.5) μBq/kg, estimated from ^{218}Po α-decays and time-coincident ^{214}Bi-^{214}Po decays, respectively, similarly to the method used in [25]. The corresponding event rates in the ROI are (71 ± 8) and (29 ± 4) events/(t × yr × keV$_{ee}$). The total ER background rate is stable throughout both science runs and measured as (82^{+5}_{-3} (sys) ± 3 (stat)) events/(t ×

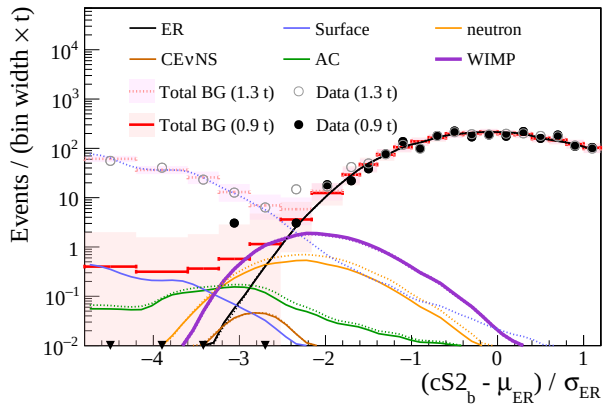

FIG. 4: Background and 200 GeV/c^2 WIMP signal best-fit predictions, assuming $\sigma_{SI} = 4.7\times10^{-47}$ cm^2, compared to DM search data in the 0.9 t (solid lines and markers) and 1.3 t (dotted lines and hollow markers) masses. The horizontal axis is the projection along the ER mean ($\mu_{\rm ER}$), shown in Fig. 3, normalized to the ER 1σ quantile ($\sigma_{\rm ER}$). Shaded bands indicate the 68% Poisson probability region for the total BG expectations.

yr × keV$_{\rm ee}$) after correcting for efficiency, which is the lowest background achieved in a dark matter detector to date.

The NR background includes contributions from radiogenic neutrons originating from detector materials, coherent elastic neutrino nucleus scattering (CEνNS) mainly from ^{8}B solar neutrinos, and cosmogenic neutrons from secondary particles produced by muon showers outside the TPC (negligible due to the muon veto [11]). The CEνNS rate is constrained by ^{8}B solar neutrino flux [26] and cross-section [27] measurements. The rate of radiogenic neutrons is modeled with GEANT4 MC [28, 29] using the measured radioactivity of materials [30], assuming a normalization uncertainty of 50% based on the uncertainty in the SOURCES 4A [31] code and the difference between the GEANT4 and MCNP particle propagation simulation codes [32]. Fast neutrons have a mean free path of ∼15 cm in LXe and produce ∼5 times more multiple-scatter than single-scatter events in the detector, allowing for background suppression. A dedicated search for multiple-scatter events finds 9 neutron candidates, consistent with the expectation of (6.4 ± 3.2) derived from the GEANT4 and detector response simulation described below, which is used to further constrain the expected single-scatter neutron event rate in DM search data.

The detector response to ERs and NRs is modeled similarly to the method described in Refs. [5, 33]. All ^{220}Rn, ^{241}AmBe, and neutron generator calibration data from both science runs are simultaneously fitted to account for correlations of model parameters across different sources and runs. To fit the ^{220}Rn data, the parameterization of the ER recombination model is improved from [5] by modifying the Thomas-Imel model [34]. These modifications include a power law field-dependence similar to [35] to account for the different drift fields in each science run, an exponential energy dependence to extend the applicability to high-energy (up to ∼20 keV$_{\rm ee}$), and an empirical energy-dependent Fermi-Dirac suppression of the recombination at low-energy ($\lesssim$ 2 keV$_{\rm ee}$). The resulting light and charge yields after fitting are consistent with measurements [33, 36–38]. The fit posterior is used to predict the ER and NR distributions in the analysis space of the DM search data, achieving an ER rejection of 99.7% in the signal reference region, as shown in Table I. ER uncertainties in (cS1, cS2$_{\rm b}$) are propagated for statistical inference via variation of the recombination and its fluctuation, as these show the most dominant effect on sensitivity (here defined as the median of an ensemble of confidence intervals derived under the background-only hypothesis [39, 40]). For WIMP signals, the uncertainties from all modeled processes are propagated into an uncertainty of 15% (3%) on the total efficiency for 6 (200) GeV/c^2 WIMPs.

TABLE I: Best-fit, including a 200 GeV/c^2 WIMP signal plus background, expected event counts with 278.8 days livetime in the 1.3 t fiducial mass, 0.9 t reference mass, and 0.65 t core mass, for the full (cS1, cS2$_{\rm b}$) ROI and, for illustration, in the NR signal reference region. The table lists each background (BG) component separately and in total, as well as the expectation for the WIMP signal assuming the best-fit $\sigma_{SI} = 4.7 \times 10^{-47}$ cm^2. The observed events from data are also shown for comparison. Although the number of events in the reference region in the 1.3 t fiducial mass indicate an excess compared to the background expectation, the likelihood analysis, which considers both the full parameter space and the event distribution finds no significant WIMP-like contribution.

Mass	1.3 t	1.3 t	0.9 t	0.65 t
(cS1, cS2$_{\rm b}$)	Full	Reference	Reference	Reference
ER	627±18	1.62±0.30	1.12±0.21	0.60±0.13
neutron	1.43±0.66	0.77±0.35	0.41±0.19	0.14±0.07
CEνNS	0.05±0.01	0.03±0.01	0.02	0.01
AC	$0.47^{+0.27}_{-0.00}$	$0.10^{+0.06}_{-0.00}$	$0.06^{+0.03}_{-0.00}$	$0.04^{+0.02}_{-0.00}$
Surface	106±8	4.84±0.40	0.02	0.01
Total BG	735±20	7.36±0.61	1.62±0.28	0.80±0.14
WIMP$_{\rm best\text{-}fit}$	3.56	1.70	1.16	0.83
Data	739	14	2	2

Energy deposits in charge- or light-insensitive regions produce lone S1s or S2s, respectively, that may accidentally coincide and mimic a real interaction. The lone-S1 spectrum is derived from S1s occurring before the main S1 in high energy events and has a rate of [0.7, 1.1] Hz. The uncertainty range is determined from differing rates of single electron S2s and dark counts in the time win-

dow before the event. The lone-S2 sample is composed of all triggered low-energy events containing S2s without a validly paired S1 and has a rate of (2.6 ± 0.1) mHz (without requiring the S2 threshold). The AC background rate and distribution are estimated by randomly pairing lone-S1s and -S2s and simulating the necessary quantities for applying the event selection defined above.

^{222}Rn progeny plate-out on the inner surface of the PTFE panels may decay and contaminate the search region if the reconstructed position falls within the fiducial mass, herein referred to as "surface" background. Decays from ^{210}Pb and its daughters that occur directly on the surface of the PTFE exhibit charge-loss due to S2 electrons being trapped on the surface and produce an S2/S1 ratio compatible with NR, as shown in Fig. 3. Several control samples are selected to derive a data-driven surface background model: DM search data reconstructed outside the TPC radius (due to position resolution) are used to predict the distribution in (cS1, cS2$_b$, Z) via a kernel density estimator; the reconstructed R distribution of surface events depends only on the size of S2 and is modeled by fitting to a control sample composed of ^{210}Po events as well as surface events with abnormally small S2/S1 from ^{220}Rn calibration and DM search data (cS1 $>$ 200 PE). The (R^2, cS2$_b$) projection in Fig. 3 shows a correlation that provides additional discrimination power in the likelihood analysis. Uncertainties in the radial shape are estimated by varying fitting methods. The normalization of the surface background is constrained by the bulk of surface events in DM search data shown in Fig. 3.

The fiducial mass, shown as a magenta line in Fig. 2, is 8.0 cm below the liquid level to avoid mis-reconstructed interactions in the GXe and 2.9 cm above the cathode to avoid interactions in this region with a larger and less-uniform electric field. The corners of the fiducial mass are restricted further by requiring that the predicted total background rate in the ROI is flat to $<10\%$ in Z across slices of R, such that the contribution from radioimpurities in detector materials to the ER background is sub-dominant relative to the uniform internal ^{214}Pb contribution. The maximum radius (42.8 cm) was chosen to expect $\lesssim 100$ surface-like events from the background model, to avoid over-constraining the corresponding tail prediction with these bulk events (Fig. 3, right). This fiducial mass contains (1.30 ± 0.01) t of LXe, determined from the total target mass of 2.00 t and the fraction of ^{83m}Kr events contained inside. An inner region containing 0.9 t mass with R $<$ 34.6 cm is shown as a blue line in Fig. 2 and is used to illustrate a reference region with negligible surface background rate. Neutron interactions in the fiducial mass occur mainly at extreme Z near the gate electrode or cathode as shown in Fig. 2, while WIMP NRs are expected to be uniformly distributed. This prompted designation of a 0.65 t core mass, marked in green in Fig. 2, which contains a significantly lower neutron rate. Table I shows the number of events predicted in these regions by the post-fit models as well as the number of observed events after unblinding.

The data in the whole 1.3 t is interpreted using an unbinned extended likelihood with profiling over nuisance parameters [41, 42]. Modeling the surface background and adding the R dimension allows for the expansion of the 1 t fiducial mass in [5] to 1.3 t, resulting in a 10% sensitivity gain. In addition to the three unbinned analysis dimensions (cS1, cS2$_b$, R), events are categorized as being inside or outside the core mass (dependent on (R, Z). All model uncertainties described above are included in the likelihood as nuisance parameters. A mis-modeling "safeguard" [43] (WIMP-like component) is added to the ER model and constrained by the ^{220}Rn calibration data. This term prevents over- or under-estimation of the ER model in the signal region due to modeling choices. The "anomalous leakage" background component used in [5] is not supported by the high statistics ^{220}Rn calibration data in SR1 and is no longer included. SR0 and SR1 are simultaneously fitted by assuming only the following parameters are correlated: electron-ion recombination in ER, neutron rate, WIMP mass and σ_{SI}. The best-fit in Fig. 4 and Table I refers to the set of parameters that maximizes the likelihood.

Confidence intervals (90% C.L.) for (σ_{SI}, mass) space were calculated by "profile construction" [39, 40] using MC simulations and the coverage was tested for different values of nuisance parameters. This unifies one- and two-sided confidence interval constructions and avoids undercoverage that can result from applying asymptotic assumptions (Wilks' theorem). This asymptotic assumption was applied in the analysis of [5] and caused a $\sim$38% (44%) decrease in the upper limit (median sensitivity) at a WIMP mass of 50 GeV/c^2. A pre-unblinding decision was made to only report two-sided intervals if the detection significance exceeds 3σ, which leads the analysis to conservatively overcover signals below the 68% sensitivity band at 50 GeV/c^2. Two independent inference codes were developed and used to cross-check the result.

Event reconstruction and selection criteria were fixed prior to unblinding. However, four aspects of the models and statistical inference were modified after unblinding cS1 $<$ 80 PE, which together caused a 2% (4%) increase in the final limit (median sensitivity). First, the ER recombination parameterization, previously described, contains improvements implemented to solve a mis-modeling of the ER background in the NR ROI. The pre-unblinding parameterization included a sharp drop at $\sim$1.5 keV$_{ee}$, which was sufficient for modeling the SR0 ^{220}Rn calibration data in [5] but caused an enhancement to the safeguard term in a post-unblinding fit of the larger statistics SR1 ^{220}Rn and DM search data. The event at low-Z and low-cS2$_b$, indicated as mostly neutron-like in Figs. 2 and 3, motivated scrutiny of the neutron model. The second modification improved this

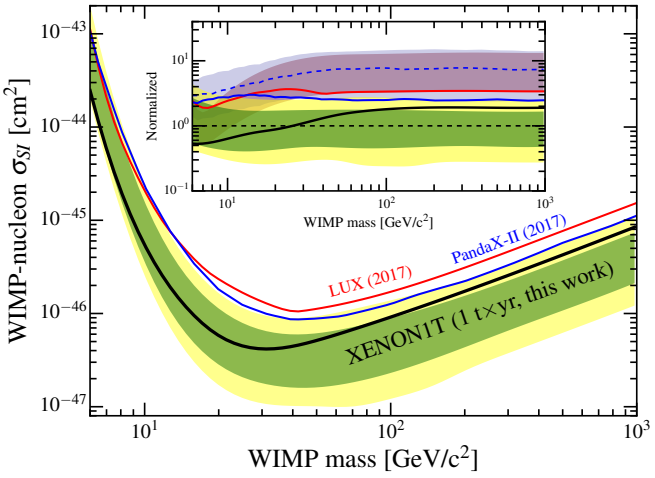

FIG. 5: 90% confidence level upper limit on σ_{SI} from this work (thick black line) with the 1σ (green) and 2σ (yellow) sensitivity bands. Previous results from LUX [6] and PandaX-II [7] are shown for comparison. The inset shows these limits and corresponding $\pm 1\sigma$ bands normalized to the median of this work's sensitivity band. The normalized median of the PandaX-II sensitivity band is shown as a dotted line.

model to correctly describe events with enlarged S1s due to additional scatters in the charge-insensitive region below the cathode. These events comprise 13% of the total neutron rate in Table I. Third, we implemented the core mass segmentation to better reflect our knowledge of the neutron background's Z distribution, motivated again by the neutron-like event. This shifts the probability of a neutron (50 GeV/c^2 WIMP) interpretation for this event in the best-fit model from 35% (49%) to 75% (7%) and improves the limit (median sensitivity) by 13% (4%). Fourth, the estimated signal efficiency decreased relative to the pre-unblinding model due to further matching of the simulated S1 waveform shape to ^{220}Rn data, smaller uncertainties from improved understanding and treatment of detector systematics, and correction of an error in the S1 detection efficiency nuisance parameter. This latter set of improvements was not influenced by unblinded DM search data.

In addition to blinding, the data were also "salted" by injecting an undisclosed number and class of events in order to protect against fine-tuning of models or selection conditions in the post-unblinding phase. After the post-unblinding modifications described above, the number of injected salt and their properties were revealed to be two randomly selected ^{241}AmBe events, which had not motivated any post-unblinding scrutiny. The number of events in the NR reference region in Table I is consistent with background expectations. The profile likelihood analysis indicates no significant excesses in the 1.3 t fiducial mass at any WIMP mass. A p-value calculation based on the likelihood ratio of the best-fit including signal to that of background-only gives $p = 0.28$, 0.41, and 0.22 at 6, 50, and 200 GeV/c^2 WIMP masses, respectively. Figure 5 shows the resulting 90% confidence level upper limit on σ_{SI}, which falls within the predicted sensitivity range across all masses. The 2σ sensitivity band spans an order of magnitude, indicating the large random variation in upper limits due to statistical fluctuations of the background (common to all rare-event searches). The sensitivity itself is unaffected by such fluctuations, and is thus the appropriate measure of the capabilities of an experiment [44]. The inset in Fig. 5 shows that the median sensitivity of this search is ∼7.0 times better than previous experiments [6, 7] at WIMP masses > 50 GeV/c^2.

Table I shows an excess in the data compared to the total background expectation in the reference region of the 1.3 t fiducial mass. The background-only local p-value (based on Poisson statistics including a Gaussian uncertainty) is 0.03, which is not significant enough, including also an unknown trial factor, to trigger changes in the background model, fiducial boundary, or consideration of alternate signal models. This choice is conservative as it results in a weaker limit.

In summary, we performed a DM search using an exposure of 278.8 days $\times 1.3$ t $= 1.0$ t×yr, with an ER background rate of $(82^{+5}_{-3}\,(\text{sys}) \pm 3\,(\text{stat}))$ events/(t × yr × keV$_{\text{ee}}$), the lowest ever achieved in a DM search experiment. We found no significant excess above background and set an upper limit on the WIMP-nucleon spin-independent elastic scattering cross-section σ_{SI} at 4.1×10^{-47} cm^2 for a mass of 30 GeV/c^2, the most stringent limit to date for WIMP masses above 6 GeV/c^2. An imminent detector upgrade, XENONnT, will increase the target mass to 5.9 t. The sensitivity will improve upon this result by more than an order of magnitude.

We gratefully acknowledge support from the National Science Foundation, Swiss National Science Foundation, German Ministry for Education and Research, Max Planck Gesellschaft, Deutsche Forschungsgemeinschaft, Netherlands Organisation for Scientific Research (NWO), NLeSC, Weizmann Institute of Science, I-CORE, Pazy-Vatat, Initial Training Network Invisibles (Marie Curie Actions, PITNGA-2011-289442), Fundacao para a Ciencia e a Tecnologia, Region des Pays de la Loire, Knut and Alice Wallenberg Foundation, Kavli Foundation, and Istituto Nazionale di Fisica Nucleare. Data processing is performed using infrastructures from the Open Science Grid and European Grid Initiative. We are grateful to Laboratori Nazionali del Gran Sasso for hosting and supporting the XENON project.

* daniel.coderre@physik.uni-freiburg.de
† pdeperio@astro.columbia.edu
‡ feigao@astro.columbia.edu

§ Also at Albert Einstein Center for Fundamental Physics, University of Bern, Bern, Switzerland
¶ Also at Kobayashi-Maskawa Institute, Nagoya University, Nagoya, Japan
** Also at Coimbra Polytechnic - ISEC, Coimbra, Portugal
†† xenon@lngs.infn.it

[1] G. Bertone, D. Hooper and J. Silk, Phys. Rep. **405**, 279 (2005).
[2] L. Roszkowski *et al.* Rep. Prog. Phys. **81**, 066201 (2018).
[3] T. Marrodán Undagoitia and L. Rauch, J. Phys. G **43**, no. 1, 013001 (2016)
[4] L. E. Strigari, Phys. Rep. **531**, 1 (2012).
[5] E. Aprile *et al.* (XENON Collaboration), Phys. Rev. Lett. **119**, 181301 (2017).
[6] D. S. Akerib *et al.* (LUX Collaboration), Phys. Rev. Lett. **118**, 021303 (2016).
[7] X. Cui *et al.* (PandaX-II Collaboration), Phys. Rev. Lett. **119**, 181302 (2017).
[8] E. Aprile *et al.* (XENON Collaboration), Eur. Phys. J. C **77**: 881 (2017).
[9] E. Aprile *et al.* (XENON Collaboration), Eur. Phys. J. C **75**: 546 (2015).
[10] P. Barrow *et al.* JINST **12**, no. 01, P01024 (2017).
[11] E. Aprile *et al.* (XENON Collaboration), JINST **9**, P11006 (2014).
[12] P. Sorensen, K. Kamdin. JINST **13**, P02032 (2018).
[13] D. Furse *et al.*. New J. Phys. **19** 053012 (2017)
[14] L. W. Kastens *et al.*, Phys. Rev. C **80**, 045809 (2009).
[15] E. Aprile *et al.* (XENON Collaboration), Phys. Rev. D **95**, 072008 (2017).
[16] R. F. Lang *et al.*, Nucl. Inst. and Meth. A **879**, 31 (2018).
[17] B. Riedel *et al.* PEARC '18, ISBN 978-1-4503-6446-1 (2018). doi:10.1145/3219104.3219155.
[18] XENON Collaboration. (2018). The pax data processor v6.8.0. Zenodo. http://doi.org/10.5281/zenodo.1195785
[19] R. Saldanha *et al.*, Nucl. Inst. and Meth. A **863**, 35 (2017).
[20] C. H. Faham *et al.*, JINST **10**, P09010 (2015).
[21] D. S. Akerib *et al.* (LUX Collaboration), JINST **12**, P11022 (2017).
[22] J. Lewin and P. Smith, Astropart. Phys. **6** 87 (1996).
[23] E. Aprile *et al.* (XENON Collaboration), Eur. Phys. J. C **77**: 275 (2017).
[24] S. Lindemann, H. Simgen, Eur. Phys. J. C **74**, 2746 (2014).
[25] E. Aprile *et al.* (XENON Collaboration), Eur. Phys. J. C **78** :132 (2018).
[26] A. M. Serenelli *et al.*, Astro. Phys. Journal **743**, 29 (2011).
[27] D. Akimov *et al.* (COHERENT Collaboration), Science **357**, 1123-1126 (2017).
[28] S. Agostinelli *et al.*, Nucl. Inst. and Meth. A **506**, 250 (2003).
[29] E. Aprile *et al.* (XENON Collaboration), J. Cosmol. Astropart. Phys. **1604**, no. 04, 027 (2016)
[30] E. Aprile *et al.* (XENON Collaboration), Eur. Phys. J. C **77**: 890 (2017).
[31] W.B. Wilson *et al.*, LANL technical note LA-13639-MS (1999).
[32] R. Lemrani *et al.*, Nucl. Inst. and Meth. A **560**, 454 (2006).
[33] E. Aprile *et al.* (XENON Collaboration), Phys. Rev. D **97**, 092007 (2018).
[34] J. Thomas, and D. A. Imel, Phys. Rev. A **36**, 614 (1987).
[35] B. Lenardo *et al.* IEEE Trans. Nucl. Sci. **62**, 3387 (2015).
[36] D. S. Akerib et al. (LUX Collaboration), Phys. Rev. D **93**, 072009 (2016).
[37] E. M. Boulton *et al.*, JINST **12**, P08004 (2017).
[38] D. S. Akerib *et al.* (LUX Collaboration), Phys. Rev. D **96**, 112011 (2017).
[39] G. J. Feldman and R. D. Cousins, Phys. Rev. D **57**, 3873 (1998).
[40] C. Patrignani *et al.* (Particle Data Group), Chin. Phys. C **40**, 100001 (2016).
[41] F. James, Comput. Phys. Commun. **20**, 29 (1980).
[42] M. S. Bartlett, Biometrika **40** 3/4 (1953).
[43] N. Priel, L. Rauch, H. Landsman, A. Manfredini, and R. Budnik, J. Cosmol. Astropart. Phys. **5** 13 (2017).
[44] J. B. Albert *et al.* (EXO-200 Collaboration), Nature **510**, 225 (2014).